CONSTRAINING THE MILKY WAY POTENTIAL WITH A SIX-DIMENSIONAL PHASE-SPACE MAP OF THE GD-1 STELLAR STREAM

Draft version January 29, 2010
Preprint typeset using LaTeX style emulateapj v. 04/20/08

CONSTRAINING THE MILKY WAY POTENTIAL WITH A 6-D PHASE-SPACE MAP OF THE GD-1 STELLAR STREAM *

Sergey E. Koposov,[1,2,3], Hans-Walter Rix[1], David W. Hogg[1,4]

Draft version January 29, 2010

ABSTRACT

The narrow GD-1 stream of stars, spanning 60 deg on the sky at a distance of ~ 10 kpc from the Sun and ~ 15 kpc from the Galactic center, is presumed to be debris from a tidally disrupted star cluster that traces out a test-particle orbit in the Milky Way halo. We combine SDSS photometry, USNO-B astrometry, and SDSS and Calar Alto spectroscopy to construct a complete, empirical 6-dimensional phase-space map of the stream. We find that an eccentric orbit in a flattened isothermal potential describes this phase-space map well. Even after marginalizing over the stream orbital parameters and the distance from the Sun to the Galactic center, the orbital fit to GD-1 places strong constraints on the circular velocity at the Sun's radius $V_c = 224 \pm 13$ km/s and total potential flattening $q_\Phi = 0.87^{+0.07}_{-0.04}$. When we drop any informative priors on V_c the GD-1 constraint becomes $V_c = 221 \pm 18$ km/s. Our 6-D map of GD-1 therefore yields the best current constraint on V_c and the only strong constraint on q_Φ at Galactocentric radii near R~ 15 kpc. Much, if not all, of the total potential flattening may be attributed to the mass in the stellar disk, so the GD-1 constraints on the flattening of the halo itself are weak: $q_{\Phi,halo} > 0.89$ at 90% confidence. The greatest uncertainty in the 6-D map and the orbital analysis stems from the photometric distances, which will be obviated by Gaia.

Subject headings: Galaxy: fundamental parameters – Galaxy: halo – Galaxy: kinematics and dynamics – surveys – stars: kinematics – stellar dynamics

1. INTRODUCTION

The Sloan Digital Sky Survey (SDSS) is an imaging and spectroscopy survey which mapped quarter of the sky near the North Galactic Cap. The data have proven extremely useful for the understanding of the Milky Way halo. In addition to a large list of MW satellites (Belokurov et al. 2007c; Koposov et al. 2007a; Irwin et al. 2007; Walsh et al. 2007) several extended stellar sub-structures in the MW halo have been found in the SDSS data, such as the tidal tail of the Palomar 5 globular cluster (Odenkirchen et al. 2001; Grillmair & Dionatos 2006a), the Monoceros ring (Newberg et al. 2002), two northern tidal arms of the disrupting Sagittarius galaxy (Belokurov et al. 2006), the so called "Orphan" stream (Grillmair 2006; Belokurov et al. 2007b), the Aquila overdensity (Belokurov et al. 2007a) and the very long thin stellar stream called GD-1 (Grillmair & Dionatos 2006b). Recently Grillmair (2009) claimed the discovery of another 4 stellar streams. Streams are presumed to be remnants of tidally disrupted satellite galaxies and clusters. They provide important insights into the history of accretion events and the physics of Galaxy formation. The tidal debris from disrupted satellites (clusters) spreads out in orbital phase on a path that is close to the orbit of the progenitor. Streams tracing out orbits therefore provide opportunities to constrain the Milky Way's gravitational potential.

After initial searches for tidal tails of globular clusters (e.g. Grillmair et al. 1995) it was the extended Sagittarius tidal tail that first made deriving such constraints practical (see e.g. Ibata et al. 2001; Helmi 2004; Johnston et al. 2005; Law et al. 2005). However, the tidal tail of the Sagittarius galaxy is quite wide and contains a considerable mixture of different stellar orbits, making it complex to model. For constraining the gravitational potential, a stellar stream that is very thin but of large angular extent, is ideal, because it permits precise orbital models.

The first studies of globular cluster tidal debris only revealed short ($\lesssim 1^\circ$) signs of tails, but in recent years with the advent of large photometric surveys such as SDSS and 2MASS and significant advances in the techniques used to find streams, significant progress has been made. The matched filter technique (Odenkirchen et al. 2001; Rockosi et al. 2002) has revealed the beautiful tidal stream of Palomar 5. Detailed analysis of the Pal 5 stream, including kinematics (Odenkirchen et al. 2001, 2003, 2009), have shown the promise of this approach, but also revealed that data over more than 10° on the sky are needed to place good constraints on the potential. Grillmair (2006), Grillmair & Dionatos (2006a,b), Grillmair & Johnson (2006) were successful in the detection of very long stellar streams using this technique, including the 63° long stellar stream GD-1 . Besides the stream length and the approximate distance, most of the properties of GD-1 were unknown. Since the stream is long but relatively thin, with no apparent progenitor

* Based on observations collected at the Centro Astronómico Hispano Alemán (CAHA) at Calar Alto, operated jointly by the Max-Planck Institut für Astronomie and the Instituto de Astrofísica de Andalucía(CSIC).

[1] Max Planck Institute for Astronomy, Königstuhl 17, 69117 Heidelberg, Germany
[2] Institute of Astronomy, Madingley Road, Cambridge CB3 0HA, UK
[3] Sternberg Astronomical Institute, Universitetskiy pr. 13, 119992 Moscow, Russia
[4] Center for Cosmology and Particle Physics, Department of Physics, New York University, 4 Washington Place, New York, NY 10003, USA

remnant, it was suggested that it arose from a globular cluster. In this paper we make an attempt to determine all possible properties of the GD-1 stream including distance, position on the sky, proper motion, and radial velocity and try to constrain the Milky Way potential using that information. This work goes in parallel with the work done by Willett et al. (2009), but we are able to get a full 6-D phase space map of the stream and are able to use that map to provide significant constraints on the MW potential. See also Eyre & Binney (2009) for theoretical discussion of using thin streams in order to constrain the MW potential.

In performing this study we have obtained the first 6-D phase-space map for a kinematically cold stellar stream in the Milky Way. We view our present analysis in same sense as a pilot study for the Gaia (Perryman et al. 2001) age, when this ESA space mission will deliver dramatically better data on streams such as GD-1.

This paper is organized as follows: In Section 2 we discuss the analysis of the SDSS photometry, which entails mapping the GD-1 stream in 3-D as well as determining its stellar population properties. In Section 3 we present the kinematics, with proper motions from SDSS-USNOB1.0 and line-of-sight velocities from SDSS and Calar Alto. In Section 4 we combine this information in an iterative step that involves improved stream membership probabilities, which in turn affects the estimates of proper motions and distances. This procedure results in the most comprehensive 6-D data set for a stellar stream in our Milky Way. In Section 5 we model the stream data by a simple orbit in a simple parametrized gravitational potential. We measure the potential circular velocity and find that the overall Milky Way potential at the GD-1 stream position is somewhat flattened, but that much of that flattening can be attributed to the disk.

2. STELLAR POPULATION OF THE STREAM

The probability that a star is a member of the GD-1 stream depends on its 6-D position and its metallicity. In the space of photometric observables, this means that it depends on (α, δ), magnitude and color. In practice, the determination of the stream's angular position, distance and metallicity (presuming it is 'old') is an iterative process which we detail here.

Grillmair & Dionatos (2006b) made the initial map of the stream using a matched color-magnitude filter based on the CMD of M13 observed in the same filters. Not presuming a particular metallicity (e.g. that of M13), we start our analysis with a simple color-magnitude box selection for stars ($0.15 < g-r < 0.41$ and $18.1 < r < 19.85$). The resulting distribution is shown in Fig. 1. That particular color-magnitude box was selected as appropriate to find metal-poor main sequence (MS) stars at a distance of $\sim$ 10 kpc, and indeed the stream is marginally discernible in the Figure. With just a color-magnitude box, however, the detection fidelity of that stream is noticeably lower than that achieved by Grillmair & Dionatos (2006b)(their Fig. 1). The distribution of stars on Figure 1 is plotted in a rotated spherical coordinate system (ϕ_1, ϕ_2), approximately aligned with the stream, where ϕ_1 is longitude and ϕ_2 is the latitude. The north pole of that coordinate system is located at α_p=34°.5987, δ_p = 29°.7331, the zero-point for

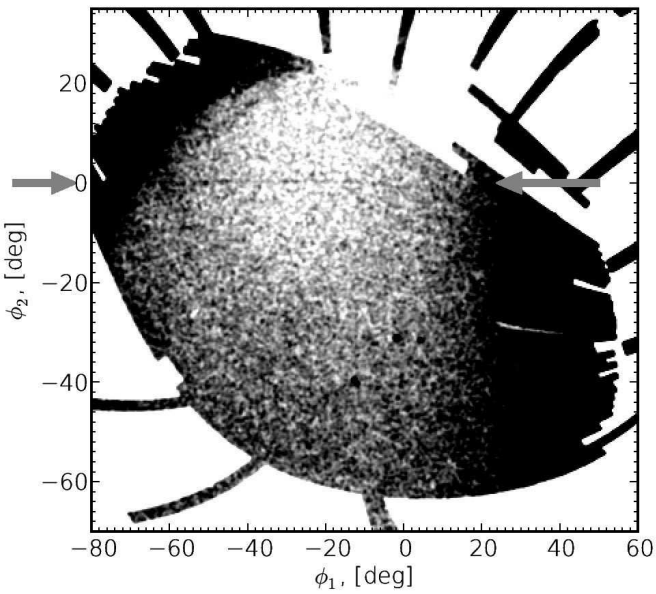

FIG. 1.— The number density of SDSS DR7 stars with $0.15 < g-r < 0.41$ and $18.1 < r < 19.85$, shown in the rotated spherical coordinate system that is approximately aligned with the GD-1 stream. The map was convolved with a circular Gaussian with $\sigma = 0.2°$. The gray arrows point to the stream, which is barely visible in this representation, extending horizontally near $\phi_2 = 0°$, between $\phi_1 = -60°$ and 0°.

ϕ_1 is located at $\alpha = 200°$, and we will use this coordinate system for convenience throughout the paper to describe stream positions (the transformation matrix from (α, δ) to (ϕ_1, ϕ_2) is given in the appendix).

If we integrate the low-contrast 2D map in Fig. 1 along the ϕ_1 axis, creating a one-dimensional profile of the stream, the presence of the stream becomes very clear. Figure 2 shows this profile for stars with $0.15 < g-r < 0.41$, $18.1 < r < 19.85$ and with $-60° < \phi_1 < -10°$. In that Figure we also overplot the Gaussian fit to this profile with $\sim$ 600 stars and Gaussian width (σ_{ϕ_2}) of $\sim 12'$. This number of stars corresponds to a total stellar mass of $M_* \approx 2 \times 10^4 M_\odot$, if we assume a distance of $\sim$ 10 kpc (see below), and a Chabrier IMF (Chabrier 2001) with an old, metal-poor stellar population. Given that number of stars, we expect to see around 3000 stream stars in SDSS with r <22. The mean surface brightness of the stream is around 29 mag/sq.arcsec.

We expand this approach to the determination of the CMD of the stream. The data and the fit shown in Figure 2 was obtained for a fairly wide color-magnitude selection box. But we can construct such a profile for any other (e.g.) color magnitude box and that profile can then be fitted by

$$N_{obs}(\phi_2|CMD) = N_{BG}(CMD) + N_{stream}(CMD) \times \frac{1}{\sqrt{2\pi}\sigma_{\phi 2}} \exp\left(-0.5\left(\frac{\phi_2 - \phi_{2,0}}{\sigma_{\phi 2}}\right)^2\right) \quad (1)$$

, where CMD refers to a given color-magnitude bin, and where we assume that both center ($\phi_{2,0}$) and width ($\sigma_{\phi 2}$) of the stream are fixed at 0 and 12 arcminutes. A fit of the Eq. 1 model to the observed data $N_{obs}(\phi_2|CMD)$ can be performed in χ^2 sense. As a result $N_{stream}(CMD)$, the number of stream stars (and its error), can be deter-

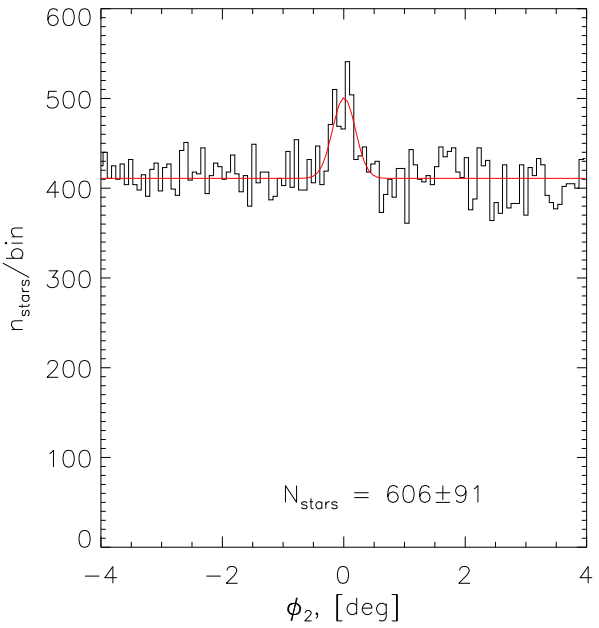

FIG. 2.— One-dimensional stellar density profile across the stream using the stars with $0.15 < g-r < 0.41$ $18.1 < r < 19.85$ across the $\phi_2 = 0°$ axis, integrated along the stream in the interval $-60° < \phi_1 < -10°$. The Gaussian fit with ~ 600 stars and σ=12′ is shown in red.

mined for each given color-magnitude bin, resulting in a Hess diagram for different pairs of SDSS filters ($u-g$, $g-r$,$r-i$, $i-z$). Figure 3 shows the resulting Hess diagram of the stream derived in several bands. These clearly show a main sequence(MS). The location of the MS turn-off cannot be clearly identified, although there may be a hint at $g = 18.5$, $u-g = 1$. On Figure 3 we also overplot the Marigo et al. (2008) isochrones with age= 9 Gyrs, $\log(Z/Z_\odot) = -1.4$ at 8.5 kpc, which seem to match quite well. Ivezić et al. (2008) recently showed that the location of MS stars in the $(u-g)-(g-r)$ color-color plane is a good metallicity diagnostic. Therefore, we construct the $(u-g)-(g-r)$ color-color diagram of the stream stellar population shown in Fig. 4, which exhibits a distinct concentration of stars at (0.8,0.3). This argues for a population of single or a dominant metallicity and we can convert this color location to a metallicity using Eq. 4 from Ivezić et al. (2008): $[Fe/H]_{phot} = -1.9 \pm 0.1$. This provides a metallicity estimate that is directly linked to SDSS spectral metallicity estimate.

To derive the metallicity, age, and distance of stream stars in a systematic way, we fit the color-magnitude diagrams using a grid of isochrones populated realistically according to the IMF (Dolphin 2002; de Jong et al. 2008). We focus on fits to the color-magnitude diagrams in u, g and g, r filters, since that the $u-g$ color of the MS turn-off is a good metallicity indicator (Ivezić et al. 2008). We create the synthetic Hess diagrams for a grid of model stellar populations (Girardi et al. 2000; Marigo et al. 2008)[6] with different ages ($3-12$ Gyr), metallicities ($Z = 0.0001-0.025$), distances ($6-14$ kpc), and a Chabrier IMF(Chabrier 2001). We then explore that grid by computing log-likelihood of the distribution of stars in color-magnitude space. Figure 5 shows the 2D profile likelihoods contours of the age vs metallicity, age vs distance and distance vs metallicity planes. The filled circle indicates the best fit model: age= 9 Gyrs, $\log(Z/Z_\odot) = -1.4$ and distance= 8 kpc. Clearly the age is the least well constrained parameter; the distance seems to be relatively well constrained, but has a covariance with [Fe/H]. We will revisit this issue later, as the analysis of Fig. 4 implies a lower metallicity. Fig. 3 shows that the isochrones are reproducing the observed Hess diagrams well, and hence further in the paper we will use t= 9 Gyrs, $\log(Z/Z_\odot) = -1.4$ as the baseline model for the stream's stellar population. It should be noted that the distance measurement from Fig. 5 represents the averaged distance along the stream from $-50° < \phi_1 < -20°$. In section 4 we will present estimates of the distance to different parts of the stream.

It is noticeable that the metallicity derived from the CMD fitting is higher than from the estimate based on empirical calibration of Ivezić et al. (2008)(see above) and higher than the measurement based on the SDSS spectra given by Willett et al. (2009). This discrepancy is understandable given the known inaccuracies of the isochrones in the SDSS photometric system (An et al. 2008). In particular the Figure 19 of An et al. (2008) paper clearly shows a mismatch between fiducial isochrone derived for the M92 globular cluster (which is used elsewhere as a good approximation of old metal-poor stars in the halo) and the theoretical isochrones. For main sequence stars below the turn-off (which are of the most interest here), the mismatch between a fiducial isochrone of the M53 globular cluster (which has metallicity [Fe/H]~ -2) from An et al. (2008) and the isochrone, which we are using can be approximated by a distance shift of $\sim 10\%$. Therefore in our analysis we reduce all the distances derived on the basis of the CMD fit by 10%. Due the these described inaccuracies with the isochrones in SDSS filters, some remaining systematic error in distances may still exist, although the study of Eyre (2009) seems to indicate it is small. Until isochrones in SDSS filters are fixed, the usage of fiducial isochrones may give more consistent results, but in the current paper we decided to proceed with the theoretical isochrones and 10% distance correction.

Splitting the CMD data into ϕ_1 bins shows that there is a distance gradient along the stream: Figure 6 shows two Hess diagrams obtained for two different pieces of the stream, on the left $-40° < \phi_1 < -20°$, and on the right -10° $< \phi_1 < 10°$. The baseline isochrone is shifted to distances of 8.5 kpc(left) and 11 kpc(right) respectively. Clearly, the part of the stream at $-10° < \phi_1 < 10°$ is further from the Sun, (as already noted by Grillmair & Dionatos 2006b; Willett et al. 2009).

The determination of the CMD properties for the stream allows us to select the possible stream member stars with much less background contamination, compared to a simple color magnitude box. Figure 7 shows the map of the stream (in ϕ_1, ϕ_2 coordinates) after applying a matched filter based on the CMD of the stream. For Fig. 7 each star in the SDSS dataset was weighted by the ratio of the stream membership probabil-

[6] To retrieve the isochrones we used the web interface provided by Leo Girardi at the Astronomical Observatory of Padua `http://stev.oapd.inaf.it/cgi-bin/cmd_2.1`

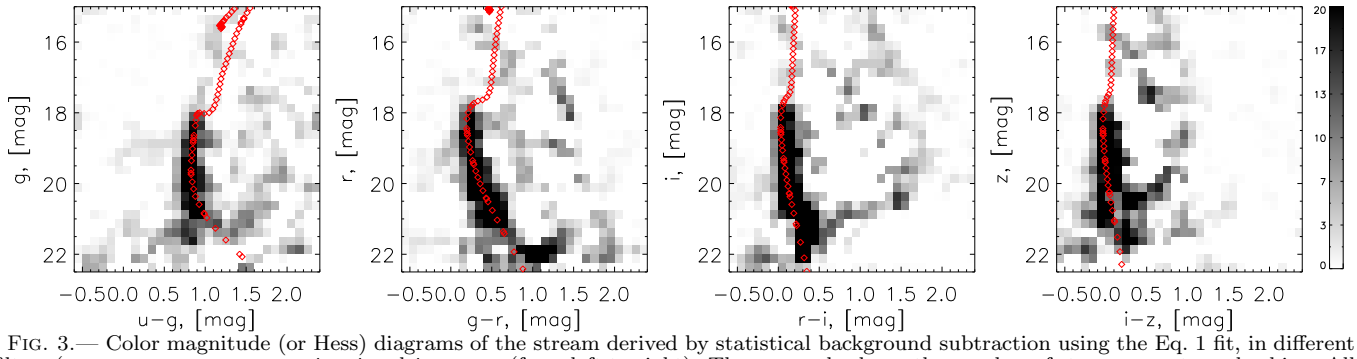

FIG. 3.— Color magnitude (or Hess) diagrams of the stream derived by statistical background subtraction using the Eq. 1 fit, in different filters ($u-g$ vs g, $g-r$ vs r, $r-i$ vs i and $i-z$ vs z (from left to right). The grayscale shows the number of stars per rectangular bins. All the magnitudes are extinction corrected. Overplotted are theoretical isochrones for age = 9 Gyrs, $\log(Z/Z_{\odot}) = -1.4$, distance = 8.5 kpc.

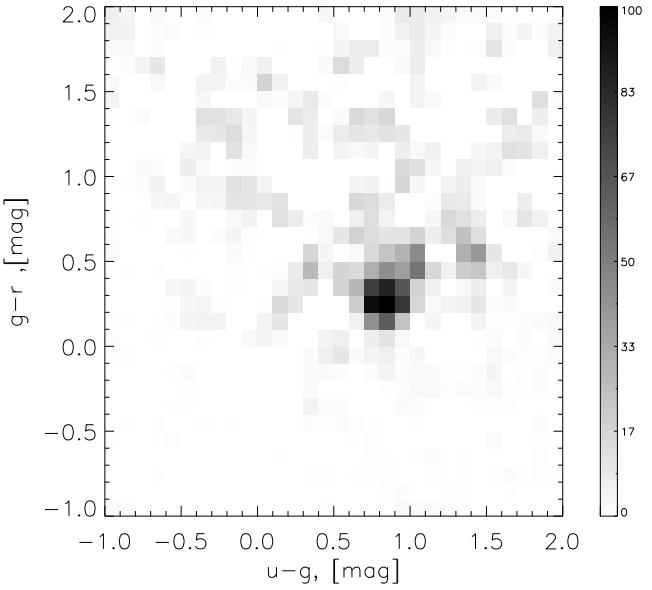

FIG. 4.— $(u-g)-(g-r)$ color-color diagram of the stream, which constitutes a photometric metallicity estimator (following Ivezić et al. 2008, Eq. 4), shown after statistical background subtraction as for Fig. 3. All the magnitudes were extinction corrected. The grayscale shows the number of stars per bin, with a distinct concentration of stars at (0.8,0.35), that implies a well defined metallicity [Fe/H] $= -1.9 \pm 0.1$.

ity and the background probability $\frac{P_{stream}(u-g,g-r,r-i,r)}{P_{BG}(u-g,g-r,r-i,r)}$,where $P_{stream}(u-g,g-r,r-i,r)$ have been computed based on the stellar population fit (Fig. 5), and $P_{BG}(u-g,g-r,r-i,r)$ was computed empirically from the regions adjacent to the stream (see e.g. Rockosi et al. 2002, for the application of similar method). The resulting image after the CMD weighting shows the stream with obviously greater contrast than Figure 1. It is noticeable that the density of stars in the stream does not seem do be constant and even does not change monotonically along the stream, instead the stream seems to have a few clumps and holes. The nature of the substructure in the stream is unclear. It may be related to either the history of the disruption process (Küpper et al. 2010), or e.g. interaction with dark matter subhalos around MW (Carlberg 2009).

3. KINEMATICS

In this section we describe how we derived estimates of the 3-D kinematics of the stream by looking at the proper motions and radial velocities of the probable stream members.

3.1. *Proper motion*

Despite the distance of $\sim$ 10 kpc to the GD-1 we demonstrate in this section that it is possible to derive good constraints on its proper motion. The analysis is based on proper motions derived from combining USNO-B1.0 (Monet et al. 2003) with SDSS data (Munn et al. 2004, 2008), which we take from SDSS DR7(Abazajian et al. 2009).

At a distance of $\sim$ 10 kpc a stream that is moving perpendicular to the line sight with the velocity of 200 km/s (roughly a characteristic velocity in the halo) should have a proper motion of the order of $\sim$ 4 mas/yr. Hence the expected proper motion is comparable to the precision of individual proper motion measurements of $3-4$ mas/yr (Munn et al. 2004). As stream member stars that are adjacent on the sky should have (nearly) identical proper motions, we can, however, determine statistical proper motions for ensembles of stars.

We start by deriving the $\vec{\mu}$-distribution of likely member stars, by extending the analysis of Section 2 and using both the angular position on the sky (specifically ϕ_2) and the location in CMDs for each star to evaluate its stream membership probability. Specifically, we grid the proper motion space into 'pixels', then we select the stars within each proper motion 'pixel' and with high membership probabilities in the CMD $(u-g,g-r,r-i,i)$ space $P_{stream}/P_{BG} \gtrsim 0.1$. For that sample of stars within each proper motion 'pixel' $(\vec{\mu},\delta\vec{\mu})$, we determine $N_{stream}(\vec{\mu}|\phi_2,CMD)$ (number of stream stars) by integrating along the stream direction ϕ_1 and fitting the resulting ϕ_2 distribution with the Eq. 1. The resulting distribution $N_{obs}(\vec{\mu})$ is shown in Fig. 8. The grayscale in the left panel of the Figure shows the proper motion distribution of μ_α, μ_δ of probable stream member stars (N_{stream}) integrated along the stream, while the contours show the proper motion distribution of the background stars selected with the same color-magnitude criteria (corresponding to N_{BG} from Eq. 1). It is clear that the stream stars are on average moving differently than the bulk of background stars. However, the observed proper motions contain the reflex motion of Sun's motion in the Galaxy. We can account for this and then convert $\vec{\mu}$ to $(\mu_{\phi_1},\mu_{\phi_2})$, the proper motion along the stream $\mu_{\phi_1} \equiv \mu_{along}$ and proper motion across the stream μ_{ϕ_2} in the Galactic rest-frame (where ϕ_1,ϕ_2 are the stream

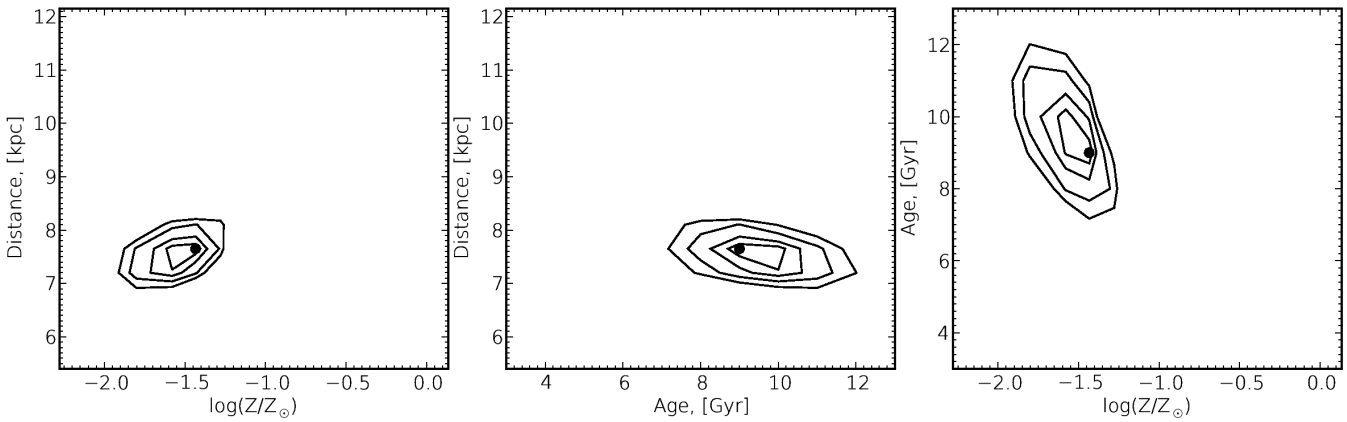

FIG. 5.— Isochrone fits to the color magnitude diagrams (Fig. 6) in u, g, r, i, z bands for the stream integrated over $-60° < \phi_1 < -10°$. The contours show the formal 60%, 90%, 99%, 99.9% confidence regions as a function of distance, age and metallicity respectively. Filled circles show the location of the best goodness of fit point.

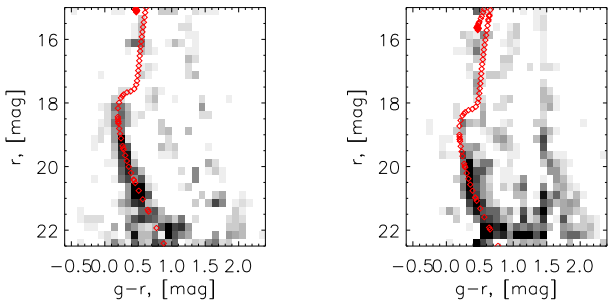

FIG. 6.— Distance variation along the stream. The CMD diagrams of the stream for two different parts of the stream, $-40° < \phi_1 < -20°$ (left), $-10° < \phi_1 < 10°$ (right). The isochrones for the the best fit model $\log(Z/Z_\odot) = -1.4$, age= 9 Gyr were shifted to the distance of 8.5 kpc on the left panel and to 11 kpc on the right panel. Some distance variation apparent, with the stellar population shown on the right located at greater distances.

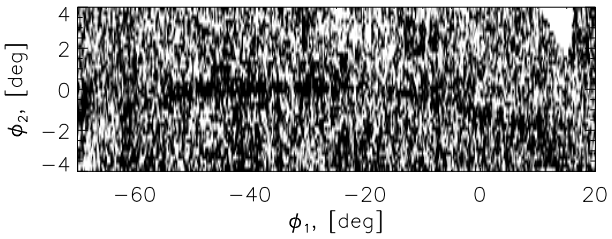

FIG. 7.— Map of stream stars in the rotated coordinate system after applying the matched CMD filter from Section 2. The figure shows the histogram of stars in ϕ_1, ϕ_2, where each star has been weighted by the CMD weight $\frac{P_{stream}(u-g,g-r,r-i,r)}{P_{BG}(u-g,g-r,r-i,r)}$. The linear variation of distance was assumed
.

coordinates introduced in Section 2). The proper motion component arising from the Sun's movement in the Galaxy can be easily computed for each star.

$$\vec{\mu}_{reflex} = \frac{1}{4.74\,|\vec{r}|}(\vec{V}_\odot - (\vec{V}_\odot \cdot \vec{r})\frac{\vec{r}}{|\vec{r}|^2})$$

where $\vec{V}$ is a 3-D velocity of the sun ($\sim$ 220 km/s) and $\vec{r}$ is the vector from the sun towards each star. As we approximately know the distance to the stream, this correction $\mu_{\phi_{1,2},c} = \mu_{\alpha,\delta} - \mu_{reflex}$ can be done. We will discuss the consequences of the uncertainties in the Sun's motion and the stream differences in Section 4.

The right panel of Fig. 8 shows the distribution of $\mu_{\phi_1}, \mu_{\phi_2}$ of the stream stars. The contours show the corresponding distribution of background stars with the similar color-magnitudes to the stream stars. Reassuringly we see that stream stars are moving approximately along ϕ_1, i.e. along the stream orbit, an important plausibility check for the correctness of the proper motion measurement. In contrast, the proper motion distribution of the background stars after subtracting the proper motion due to sun's movement is centered around $(\mu_{\phi_1}, \mu_{\phi_2}) = (0, 0)$, which appears reasonable since with our color-magnitude selection we are selecting primarily the halo stars at distances $\sim$ 10 kpc. Those show little net rotation(Carollo et al. 2007; Xue et al. 2008). The estimate $\langle \mu_{\phi_1} \rangle \approx -8$ mas/yr also immediately implies that the stream is going retrograde with respect to the Milky Way's disk rotation.

In Figure 9 we illustrate the proper motion variation along the stream. These plots, showing only $\mu_{\phi_1}(\phi_1)$ were derived the same way as Fig. 8, except that we did not integrate in ϕ_1 along the entire stream but only in ϕ_1 intervals. The right panel of Fig. 9 shows the distribution of the proper motions along the stream of the background stars. The left panel of the Figure shows the distribution of proper motions of likely stream member stars as a function of angle along the stream (the proper motion due to the Sun's motion was subtracted). The left panel reveals a slight, but significant gradient in $\langle \mu_{\phi_1} \rangle$, of the order of 3 to 5 mas/yr. Note that the decrease of the proper motions towards $\phi_1 = 0$ coincides with the distance increase to the stream (see Fig. 6).

Having determined the stream proper motions, we can further improve the CMD-filtered map of the GD-1 stream (Fig. 7) by requiring that the proper motions of the stars are consistent with the proper motion of the stream. That is shown in Fig. 10. and discussed in Section 3.2.

3.2. *Radial velocities*

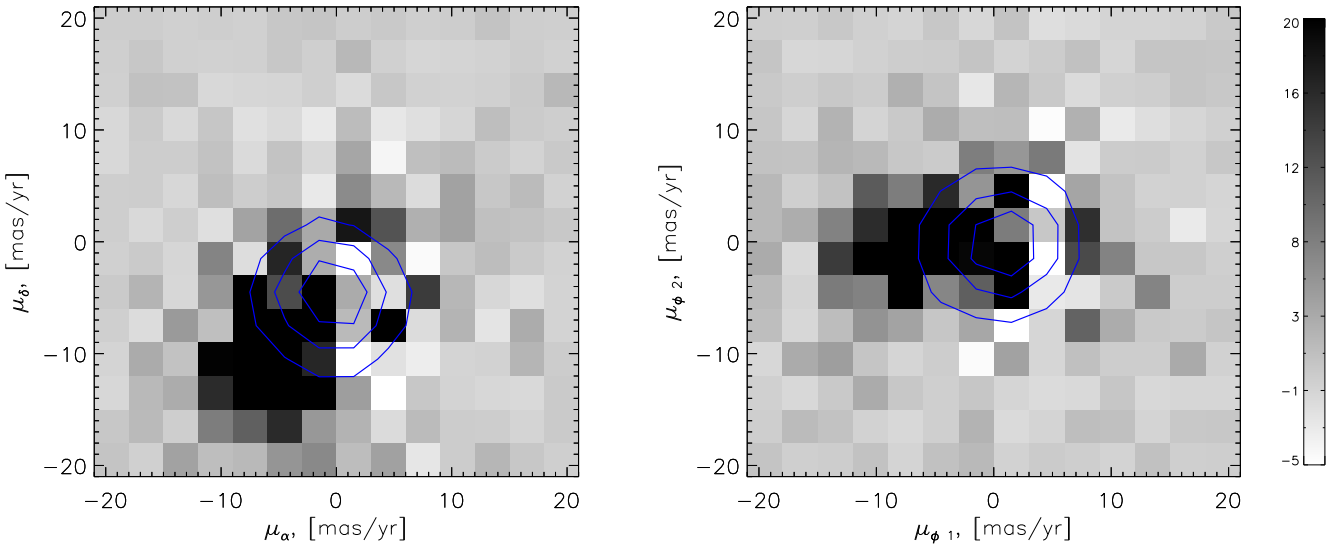

FIG. 8.— Proper motion of the stream. The left panel shows the proper motion in right ascension and declination μ_α, μ_δ (as observed, e.g. no correction for the Solar motion in the Galaxy was made). The right panel shows the proper motion in the rotated coordinate system (ϕ_1, ϕ_2) (ϕ_1 is oriented along the stream) and after the subtraction of the proper motion due to the Sun's motion in the Galaxy (assuming for now $V_c = 220$ km/s). The grayscale in each of the panels shows the number of stars per proper motion bin. Contours corresponding to 30,60,90 stars per bin show the the proper motion distribution for the field stars. with similar colors and magnitudes to the stream stars. The proper motions of the stream stars are clearly distinguishable from the proper motions of the background stars. The right panel confirms the fact that the stream stars are moving approximately along its orbit ($\mu_{\phi_2} \approx 0$ mas/yr), while the mean proper motions of background stars after subtracting Sun's motion are consistent with zero.

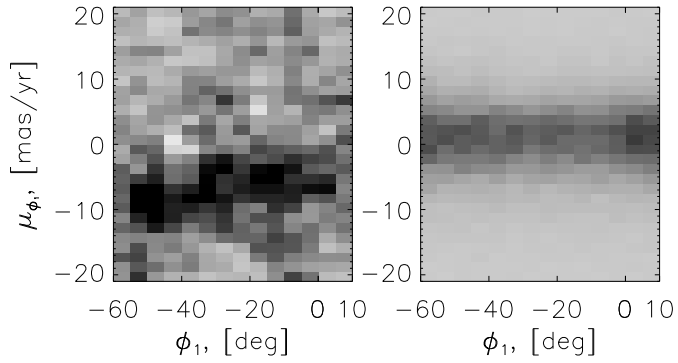

FIG. 9.— Variation of the proper motions along the stream (corrected for the Solar reflex motion, assuming $V_0 = 220$ km/s). The left panel shows the distribution of μ_{ϕ_1} for the stream candidate stars as a function of ϕ_1. The right panel shows the distribution of μ_{ϕ_1} of the field stars selected using the same color-magnitude criteria as the stream stars. The variation of proper motions of stream stars with ϕ_1 is clearly visible in the left panel. Near $\phi_1 \sim 0°$ the proper motion of the stream is around -5 mas/yr, while at $\phi_1 \sim -50°$ it is around -8 mas/yr (corresponds to ~ 300 km/s at 8 kpc).

To construct the 6-D phase space distribution of the stream, the radial velocities are the remaining datum. By necessity the actual sample for which spectra, and hence radial velocities, will be available, will differ from the photometric sample just described. In this section we will use both the data from the SDSS/SEGUE survey (Yanny et al. 2009) as well as radial velocities obtained by us with the TWIN spectrograph on Calar Alto, specifically targeting likely stream member stars.

3.2.1. *SDSS radial velocities*

SEGUE and SDSS only provide sparse spatial sampling of high latitude stars. SEGUE did not target any GD-1 member stars specifically. Therefore we have to search through the existing SEGUE spectra to identify likely, or possible, member stars by position on the sky, CMD position and proper motion. In the previous section we described that we used the ratio of the stream/background probabilities $\frac{P_{stream}(u-g,g-r,r-i,r)}{P_{BG}(u-g,g-r,r-i,r)}$ to select high probability members of the stream. Now additionally to that we also select the stars within the μ_α, μ_δ box (see Fig. 8). That allows us to have a sample of stream stars with much less background contamination, although the overall size of that sample is significantly smaller, since the the SDSS/USNO-B1.0 measurements of the proper motions were done for stars with $r \lesssim 20$(Munn et al. 2004). To illustrate how good the proper motion selection is when combined with the color-magnitude selection we show map of high probability stream member stars on Figure 10. The stream is now clearly seen in individual stars. In Figure 10 we also overplot the location of existing SEGUE DR7 pointings, some of which cover the stream. Therefore we may expect to find some stream members among the SEGUE targets in these fields.

Figure 11 shows the SDSS/SEGUE radial velocity distribution as a function of ϕ_1 for those stars whose proper motions and color-magnitude position are consistent with stream membership, and which are located within 3 degrees from the center of the stream. The typical uncertainty of the SDSS/SEGUE radial velocities is $\sim$20 km/s. The filled red circles in this Figure show the subset of stars located within 0°.3 from the center of the stream and therefore represent the subset with very high membership probability, while the open black circles represent(spatially selected, $|\phi_2| > 0.3°$) background stars with similar proper motion and color magnitude. The filled symbols in Fig. 11 clearly de-

lineate the radial velocity of the stream. Clumps of red circles are visible at (ϕ_1, V_{rad})≈(-25°,-100 km/s), (-30°,-80 km/s), (-47°,0 km/s), (-55°,40 km/s). In order to perform the formal measurements of the radial velocities we performed a maximum likelihood fit by a model, consisting from two Gaussians one (wide) Gaussian was representing the background distribution, while the second (narrow) was modeling velocity distribution of stream stars. This fit gave us the following results: (ϕ_1, V_{rad})=(-56°,39±14 km/s), (-47°,-7±10 km/s), (-28°,-61±6 km/s), (-24°, -83±9 km/s).

3.2.2. *Calar Alto radial velocities*

Since the SDSS/SEGUE radial velocities only provide constraints at a few points of the stream, we decided to obtain additional radial velocity information with targeted observations. We based the target selection for likely stream members on all the available information discussed in the previous sections: position on the sky, color-magnitude location and proper motions. We selected 34 stars likely members with $r \lesssim 19$ for the observations. All these stars are within the sample plotted in the Figure 10. These stars are mostly main-sequence and main-sequence turn-off stars with $18 \lesssim r \lesssim 19$.

The observations were performed the TWIN spectrograph on the 3.5m telescope at Calar Alto observatory, during several nights of service observing in February 2009. The TWIN spectrograph is the intermediate resolution spectrograph installed in the Cassegrain focus of the telescope. It consists from two separate spectroscopic channels (blue and red) behind the common entrance slit. The light from the slit is splitted into "red" and "blue" beams by a dichroic mirror. We used the blue and red arms of the spectrograph at a resolution of $4000-5000$ to observe the H_β, Mgb lines and CaII near-IR triplet respectively. The standard data reduction steps were applied to the dataset using custom written routines in Python language. The median signal to noise ratio per pixel was 7 for the blue spectra and 3 for red spectra.

We used both the blue and the red spectra to compute the radial velocity of each star. The radial velocity of each star was derived by minimizing χ^2 as a function of velocity shift of the template convolved with the appropriate Line Spread Function (LSF). The χ^2 for each star was a sum of the χ^2 for the blue and the red part of the spectra. As template in the blue spectral range we used the spectra from the ELODIE database (Prugniel et al. 2007) for stars of similar color and magnitude to the targeted ones and with low metallicity [Fe/H] ~ -2. In the red spectral range the template spectra was simply consisting from three lines of Ca triplet at 8498.02Å, 8542.09Å and 8662.14Å. The error of each velocity measurement was determined using the condition $\Delta(\chi^2(V)) = 1$.

The Calar Alto measurements of the velocities together with their errors are overplotted in blue symbols in Fig. 11. It is apparent from Fig. 11 that for $-50° < \phi_1 < -10°$ the targeting strategy was very successful, nicely delineating the projected velocity gradient along the stream. Overall out of 34 observed stars ~ 24 stars belong to the stream and ~ 5 didn't have enough S/N for the velocity determination. Unfortunately the targeting near $\phi_1 \approx +5°$ failed to identify stream members, probably because the stream there is less intense and further away.

4. MODELING

In the previous section we described the derivation of different stream properties such as distance, position on the sky, proper motion separately. In this Section we will map the stream in 6-D position-velocity space in a more consistent way, using all the available information (see e.g. Cole et al. 2008, for the application of similar, although simpler method to Sgr stream). This will provide us with a set of orbit constraints along different sections of the GD-1 stream, which we will then model by an orbit to derive potential constraints.

4.1. *Positions on the sky and distances to the stream*

We start by characterizing the projected stream position and its distance from the Sun through a maximum likelihood estimate for a parametrized model of the stream $P_{stream}(r, g-r, \phi_1, \phi_2)$ that describes it in 4-dimensional space of photometric observables r,$g-r$,ϕ_1,ϕ_2:

$$P_{stream}(r, g-r, \phi_1, \phi_2) = \mathrm{CMD}(r, g-r, D(\phi_1)) \times$$
$$\times I(\phi_1) \times \frac{1}{\sqrt{2\,\pi}\sigma_{\phi_2}(\phi_1)} \exp\left(-\frac{(\phi_2 - \phi_{2,0}(\phi_1))^2}{2\,\sigma^2_{\phi_2}(\phi_1)}\right) \quad (2)$$

Here $\phi_{2,0}(\phi_1)$ is the ϕ_2 position of the stream center on the sky as a function of ϕ_1, $\sigma_{\phi_2}(\phi_1)$ is the projected width of the stream in ϕ_2, $I(\phi_1)$ is the "intensity" (i.e. the number density) of the stream as a function of ϕ_1, and $D(\phi_1)$ is the distance to the stream. Further, $CMD(r, g-r, D(\phi_1))$ is the normalized Hess diagram (i.e. the probability distribution in CMD space) expected for the stream's stellar population at a distance of $D(\phi_1)$ after accounting for the observational errors. We construct that CMD based on the age and metallicity obtained in Section 2 and the isochrones from Girardi et al. (2000); Marigo et al. (2008) (assuming that $\frac{d[Fe/H]}{d\phi_1}$=0 and $\frac{d(age)}{d\phi_1}$=0). In this model, P_{stream} depends on four functions – $I(\phi_1)$, $\phi_{2,0}(\phi_1)$, $\sigma_{\phi_2}(\phi_1)$, $D(\phi_1)$ – which we take to be piecewise constant; i.e. for intervals $\delta\phi_1$ they simply become four parameters.

For the field stars, $P_{BG}(r, g-r, \phi_1, \phi_2)$ the analogous 4D distribution is

$$P_{BG}(r, g-r, \phi_1, \phi_2) = I_{BG}(\phi_1, \phi_2) \times CMD_{BG}(r, g-r, \phi_1)$$

, where $I_{BG}(\phi_1, \phi_2)$ is the 2D number density distribution of the field stars around the stream and $CMD_{BG}(r, g-r, \phi_1)$ the corresponding color-magnitude diagram. These functions are determined empirically from the data in parts of the sky adjacent to the stream ($|\phi_2| \gtrsim 0.5°$). $I_{BG}(\phi_1, \phi_2)$ is determined by fitting the density of the stars in the ϕ_1, ϕ_2 space by a polynomial. $CMD_{BG}(r, g-r, \phi_1)$ is determined by constructing the Hess diagrams using all the stars with $0.3° < |\phi_2| < 5°$ in several ϕ_1 bins.

To simplify the determination of $P_{BG}(r, g-r, \phi_1, \phi_2)$ and $P_{stream}(r, g-r, \phi_1, \phi_2)$, we split the stream in several ϕ_1 pieces, and consider $I(\phi_1)$, σ_{ϕ_2}, $D(\phi_1)$ and $\phi_{2,0}(\phi_1)$ as constants within them. The log-likelihood for the mixture of the P_{stream} and P_{BG} distribution can be written

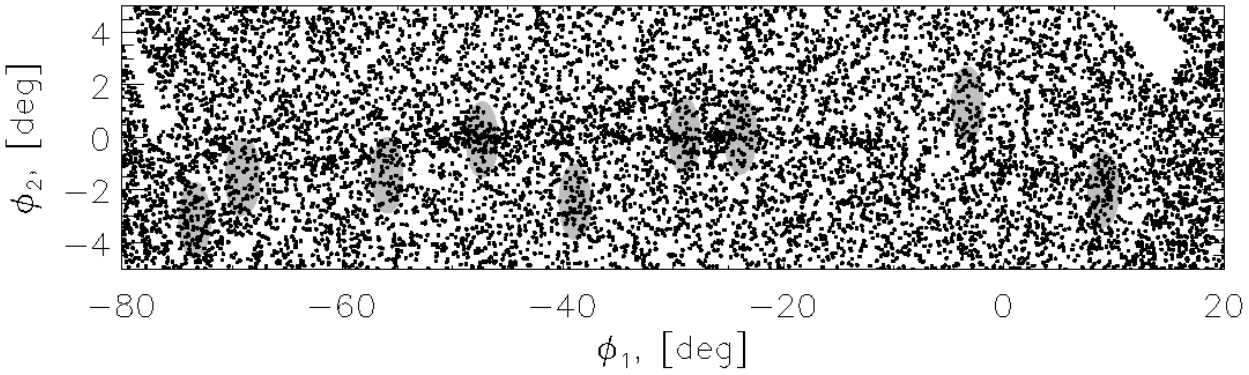

FIG. 10.— Stars that match the expectations for stream members with regards to proper motions (-15 mas/yr$< \mu_{\phi_1} < -5$ mas/yr, $|\mu_{\phi_2}| < 3$ mas/yr), colors and magnitudes (but no ϕ_2 filter), used in the candidate selection for radial velocity measurements. The stream can be clearly seen in distribution of individual stars. The locations of the SEGUE DR7 pointings are shown by gray circles.

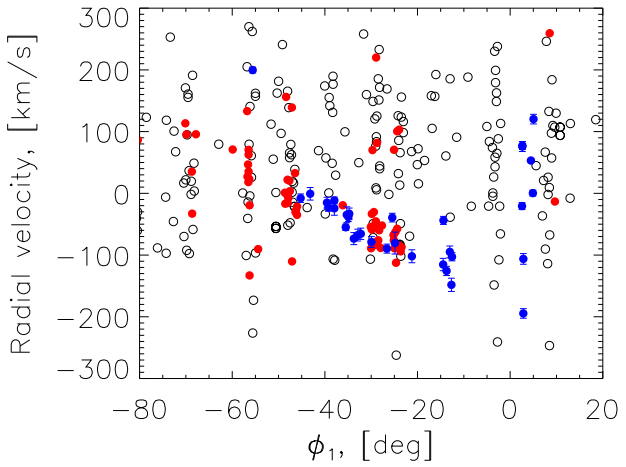

FIG. 11.— Radial velocities of likely stream stars (filled circles). The Figure shows the radial velocities drawn from the SDSS/SEGUE (red circles) and Calar Alto spectra (blue circles). The red and blue symbols reflect the radial velocities of all stars matching in color, magnitude and proper motion that have positions with $|\phi_2| < 0.3°$. The open circles represent SDSS/SEGUE velocities of similar stars but with $|\phi_2| > 0.3°$. The radial component of the Solar reflex motion (taking $V_0 = 220$ km/s) was subtracted from all datapoints.

as (here for convenience we introduce α as a fraction of stream stars instead of $I(\phi_1)$):

$$\ln(\mathcal{L}) = \sum_{stars} 2\ln(\alpha\, P_{stream}(r_i, g_i - r_i, \phi_{1,i}, \phi_{2,i}) + (1-\alpha) P_{BG}(r_i, g_i - r_i, \phi_{1,i}, \phi_{2,i})) \quad (3)$$

and should be maximized with respect to the parameters (σ_{ϕ_2}, $D(\phi_1)$, $\phi_{2,0}(\phi_1)$ and α). The maximization is performed using the Truncated Newton method(Nash 1984). The parameter errors are obtained using numerically computed Fisher information (see e.g. Cox & Hinckley 1974).

The left and central panels of Figure 12 show the resulting estimates of the projected position and the distance of the stream, the parameters used in the subsequent orbit fitting. We do not use the number density of stream stars, as it varies noticeably along the stream (see Fig. 7) and the reason of these variations is not clear. It is apparent from Fig. 10 that the projected stream position is very well defined, and that a distance gradient exists along the stream.

4.2. *Proper motions*

The likelihood maximization just described also results in stream membership probabilities for any given star i, $P_{stream}(r_i, g_i - r_i, \phi_{1,i}, \phi_{2,i})$. This information can then be used to estimate via maximum likelihood the mean proper motions of different stream pieces, thereby extending the observational estimates to the full 6-D space (r,$g-r$,ϕ_1,ϕ_2,μ_{ϕ_1},μ_{ϕ_2}).

$$P_{stream,\mu}(r, g-r, \phi_1, \phi_2, \mu_{\phi_1}, \mu_{\phi_2}) = P_{stream}(r, g-r, \phi_1, \phi_2) \times \frac{1}{2\,\pi\,\sigma_\mu^2} \times \exp\left(-\frac{(\mu_{\phi_1} - \mu_{\phi_1,0}(\phi_1))^2 + (\mu_{\phi_2} - \mu_{\phi_2,0}(\phi_1))^2}{2\,\sigma_\mu^2}\right) \quad (4)$$

where we simply take the previously determined P_{stream} as a prior, to be modified by the Gaussian distribution in the 2D proper motions space. Here, the proper motion distribution is characterized by three functions, $\mu_{\phi_1,0}(\phi_1)$, $\mu_{\phi_2,0}(\phi_1)$ and σ_μ, which again we take to be piecewise constant. The distribution of the background stars in the 6-D space $P_{BG,\mu}(r, g-r, \phi_1, \phi_2, \mu_{\phi_1}, \mu_{\phi_2})$ is obtained empirically by binning the observational data. Then we construct again the logarithm of likelihood, considering variations in four parameters: the number of stream stars, the proper motion of the stream in ϕ_1 and ϕ_2 and the proper motion spread σ_μ. This likelihood is then maximized and we determine the μ_{ϕ_1}, μ_{ϕ_2} and σ_μ for different stream pieces. The right panel of the Figure 12 shows the resulting proper motion estimates as a function of ϕ_1. These proper motions have not been corrected here for the Sun's reflex motion, which we will model in Section 5.

Overall, the analysis presented in the previous sections has resulted in the best and most extensive set of 6-D phase-space coordinate map for a cold stream of stars in

TABLE 1
Radial velocities from the Calar Alto Observations

Star	ϕ_1 [deg]	ϕ_2 [deg]	V_{rad} [km/s]
SDSS J094105.35+315111.6	−45.23	−0.04	28.8 ± 6.9
SDSS J094705.26+332939.8	−43.17	−0.09	29.3 ± 10.2
SDSS J095740.48+362333.0	−39.54	−0.07	2.9 ± 8.7
SDSS J095910.43+363206.6	−39.25	−0.22	-5.2 ± 6.5
SDSS J100222.01+374113.3	−37.95	0.00	1.1 ± 5.6
SDSS J100222.02+374049.2	−37.96	−0.00	-11.7 ± 11.2
SDSS J101033.02+393300.8	−35.49	−0.05	-50.4 ± 5.2
SDSS J101110.08+394453.9	−35.27	−0.02	-30.9 ± 12.8
SDSS J101254.83+395525.6	−34.92	−0.15	-35.3 ± 7.5
SDSS J101312.05+400613.3	−34.74	−0.08	-30.9 ± 9.2
SDSS J101702.15+404747.3	−33.74	−0.18	-74.3 ± 9.8
SDSS J101951.76+412701.5	−32.90	−0.15	-71.5 ± 9.6
SDSS J102216.20+415534.7	−32.25	−0.17	-71.5 ± 9.2
SDSS J103003.87+434351.7	−29.95	−0.00	-92.7 ± 8.7
SDSS J104341.92+460224.7	−26.61	−0.11	-114.2 ± 7.3
SDSS J104840.98+464922.1	−25.45	−0.14	-67.8 ± 7.1
SDSS J105036.96+472000.1	−24.86	0.01	-111.2 ± 17.8
SDSS J110711.27+494415.9	−21.21	−0.02	-144.4 ± 10.5
SDSS J114242.08+533841.4	−14.47	−0.15	-179.0 ± 10.0
SDSS J114724.59+535546.8	−13.73	−0.28	-191.4 ± 7.5
SDSS J115116.08+542142.7	−13.02	−0.21	-162.9 ± 9.6
SDSS J115326.06+542930.6	−12.68	−0.26	-217.2 ± 10.7
SDSS J115404.06+543511.4	−12.55	−0.23	-172.2 ± 6.6

TABLE 2
Stream positions

ϕ_1 [deg]	ϕ_2 [deg]
−60.00	-0.64 ± 0.15
−56.00	-0.89 ± 0.27
−54.00	-0.45 ± 0.15
−48.00	-0.08 ± 0.13
−44.00	0.01 ± 0.14
−40.00	-0.00 ± 0.09
−36.00	0.04 ± 0.10
−34.00	0.06 ± 0.13
−32.00	0.04 ± 0.06
−30.00	0.08 ± 0.10
−28.00	0.03 ± 0.12
−24.00	0.06 ± 0.05
−22.00	0.06 ± 0.13
−18.00	-0.05 ± 0.11
−12.00	-0.29 ± 0.16
−2.00	-0.87 ± 0.07

TABLE 3
Stream distances

ϕ_1 [deg]	Distance [kpc]
−55.00	7.20 ± 0.30
−45.00	7.59 ± 0.40
−35.00	7.83 ± 0.30
−25.00	8.69 ± 0.40
−15.00	8.91 ± 0.40
0.00	9.86 ± 0.50

the Milky Way.

5. ORBIT FITTING

If we can assume that all the stream stars lie close to one single test-particle orbit, then our phase space map of the GD-1 stream should not only define this orbit, but at the same time constrain the Milky Way's potential. In general the stars in the tidal stream have slightly different energies and angular momenta, but the assumption that the stream stars are moving along the same orbit is plausible , especially if the stream is thin and is near pericenter (Dehnen et al. 2004, & private communication). But it is not straightforward to quantify the quality of such an approximation. For now we simply fit an orbit to our 6-D map of available observational data: the position on the sky, $\phi_2(\phi_1)$, proper motion $\vec{\mu}(\phi_1)$, distance to the stream $D(\phi_1)$ and radial velocity $V_{rad}(\phi_1)$. For each assumed potential, we will determine the best fit orbit, but then marginalize over the orbits to determine the range of viable gravitational potentials. This analysis extends earlier efforts by Grillmair & Dionatos (2006b) and Willett et al. (2009) who have presented orbit solutions for GD-1 . However, we can now draw on a much more extensive set of observational constraints. We also explore the fit degeneracies. Given that our 6-D phase-space map of the GD-1 stream spans only a limited range in R and z (as seen from the Galactic center 11 kpc$\lesssim$R$\lesssim$ 14 kpc, 5 kpc$\lesssim$z$\lesssim$ 9 kpc) it proved useful to consider very simple parametrized potentials at first. Further it proved necessary to consider what prior information we have on the Sun's (i.e. the observers) position and motion, as well as on our Milky Way's stellar disk mass.

TABLE 4
Stream proper motions

ϕ_1 [deg]	μ_{ϕ_1} [mas/yr]	μ_{ϕ_2} [mas/yr]	σ_μ [mas/yr]
-55.00	-13.60	-5.70	1.30
-45.00	-13.10	-3.30	0.70
-35.00	-12.20	-3.10	1.00
-25.00	-12.60	-2.70	1.40
-15.00	-10.80	-2.80	1.00

5.1. *One component potential*

The stream is located at Galactocentric $(R, z) \approx (12, 6)$ kpc, a regime where presumably both the stellar disk and the dark halo contribute to the potential , and its flattening. Of course, the stream dynamics are solely determined by the total potential, and therefore we consider first a simple single-component potential, the flattened logarithmic potential

$$\Phi(x, y, z) = \frac{V_c^2}{2} \ln\left(x^2 + y^2 + \left(\frac{z}{q_\Phi}\right)^2\right), \qquad (5)$$

which has only two parameters: the circular velocity V_c and the flattening q_Φ. Note that $(1-q_{density}) \approx 3(1-q_\Phi)$ for moderate flattening (e.g. p.48 of Binney & Tremaine 1987). Such a simple potential seems justified as the stream stars are only probing a relatively small range in R and z.

In practice, we fit an orbit to the 6-D stream map by considering a set of trial starting points in the Galaxy, specified by the initial conditions $(\vec{X}(0), \dot{\vec{X}}(0))$ in standard Cartesian Galactic coordinates. Together with an assumed gravitational potential this predicts $(\vec{X}(t), \dot{\vec{X}}(t))$, which can be converted to the observables, $\phi_2(\phi_1)$, $\vec{\mu}(\phi_1)$, $D(\phi_1)$, $V_{rad}(\phi_1)$ and then compared to the

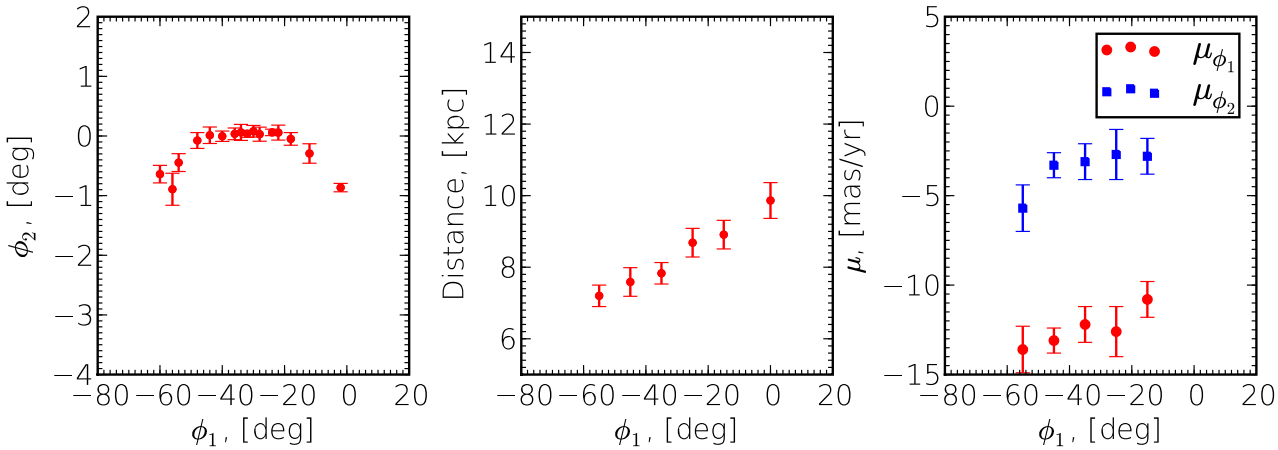

FIG. 12.— Summary of photometrically derived stream properties based on maximum likelihood fits to chunks of the stream, drawing on SDSS photometry and astrometry (see Section 4). The left panel shows the positions of the stream on the sky in ϕ_1,ϕ_2 coordinates. The middle panel show the measurements of the distances as a function of ϕ_1. The right panel shows the statistical proper motions of the stream stars (without the correction for the Solar motion); red circles show the μ_{ϕ_1} (the proper motion along the stream), blue squares show the μ_{ϕ_2} (the proper motion perpendicular to the stream).

6-D observations (Fig. 13). For each $[(\vec{X}(0), \dot{\vec{X}}(0)|\Phi(\vec{X})]$ we can evaluate the quality of the fit by calculating χ^2, summing over all data points, shown in Fig. 13. For any given $\Phi(\vec{X})$, χ^2 can be then minimized with respect to the orbit, i.e. $(\vec{X}(0), \dot{\vec{X}}(0))$, providing the 'best fit' orbit in this potential and the plausibility of that potential. The minimization is performed using the MPFIT code (Markwardt 2009) implementing the Levenberg-Marquardt technique (Marquardt 1963) translated into Python[7]. The data used to constrain the potential are given in the Tables 1, 2, 3, 4 (except the SDSS measurements of the radial velocities which are given in the end of Section 3).

It is crucial to note that the conversion of $(\vec{X}(t), \dot{\vec{X}}(t))$ to the space of observables depends on the position and motion of the observer, i.e. on distance from the Sun to the Galactic center (R_0) and on the 3-D velocity of the Sun in the Galaxy rest-frame ($\vec{V}_0$). At this stage we adopt $R_0 = 8.5$ kpc based on recent determinations (e.g. Ghez et al. 2008; Gillessen et al. 2009), but later we will relax this. The second parameter $\vec{V}_0 \equiv \vec{V}_{LSR} + \Delta\vec{V}_{LSR}$ (where V_{LSR} is the velocity of the Local Standard of Rest and $\Delta\vec{V}_{LSR}$ is the Sun's velocity relative to the LSR) is linked to the fitting not only through conversion of the observable relative stream velocities to the GC rest system, but also conceptually through the plausible demand that $\Phi(\vec{X})$ and in particular $V_c(R_0, 0)$ also reproduces $\vec{V}_{LSR}$. In this way, constraints on the potential flattening can be derived by considering $r\frac{d\Phi}{dr}$ in the disk plane ($\vec{V}_{LSR}$) and the plane of the GD-1 stream. The velocity of the Sun relative to the Local Standard of Rest (LSR) $\Delta\vec{V}_{LSR}$ is quite well known from the HIPPARCOS measurements (Dehnen & Binney 1998): $\Delta\vec{V}_{LSR}[km/s] = 10\vec{e}_x + 5.25\vec{e}_y + 7.17\vec{e}_z$. The velocity of the LSR, i.e. $V_c(R_0, 0)$ has a considerable uncertainty (Brand & Blitz 1993; Ghez et al. 2008; Xue et al. 2008; Reid et al. 2009). Initially we will consider the velocity of the LSR simply a consequence of the assumed potential, i.e. $V_{LSR} \equiv V_c(R_0, 0)$.

Figure 13 illustrates the result of such fitting, by overplotting the best fit orbit for the plausible potential with $V_c = 220$ km/s and $q_\Phi = 0.9$ over observational data. It is clear that even for the simple flattened logarithmic potential, an orbit can be found that reproduces the observables well. This fit and Figure serve to illustrate a few generic points that also hold for orbit fits in differing potentials: the stream moves on a retrograde orbit and it is near pericenter, where the stream is expected to approximate an orbit well (Dehnen et al. 2004). After fitting a first orbit, we may also note its global parameters (see Fig. 17 for a 3-D map of the orbit): pericenter is at 14 kpc from the GC; apocenter is at 26 kpc; and the inclination is 39°.

For any given potential $\Phi(\vec{X}|V_c, q_\Phi)$ we can find best-fit orbit by marginalizing over $(\vec{X}(0), \dot{\vec{X}}(0))$ to see what our 6-D map of GD-1 implies about the relative plausibility of different V_c and q_Φ: Figure 14 shows the log-likelihood surface for the potential parameters (V_c, q_Φ); note again that this fit neglects all other prior information on V_c at the Sun's position. The contours show 1σ, 2σ, 3σ confidence regions on the parameters, derived from the $\delta(\ln(\mathcal{L}))$ values for two degrees of freedom (i.e. a two parameter fit)(see e.g. Lampton et al. 1976). The insets at the left and bottom show the marginalized distributions for single parameters. The best fit values with the 2-sided 68% confidence intervals are $V_c = 221^{+16}_{-20}$ km/s and $q_\Phi = 0.87^{+0.12}_{-0.03}$. Figure 14 illustrates that the flattening parameter q_Φ is quite covariant with the equatorial circular velocity V_c. An extreme example may serve to explain this covariance qualitatively. If the stream went right over the pole (z-axis), then the local force gradient would be proportional to $V_c \times q_\Phi$ (Eq. 5). Information about the potential flattening must therefore come from combining kinematics and dynamics in the disk plane

[7] http://code.google.com/astrolibpy/

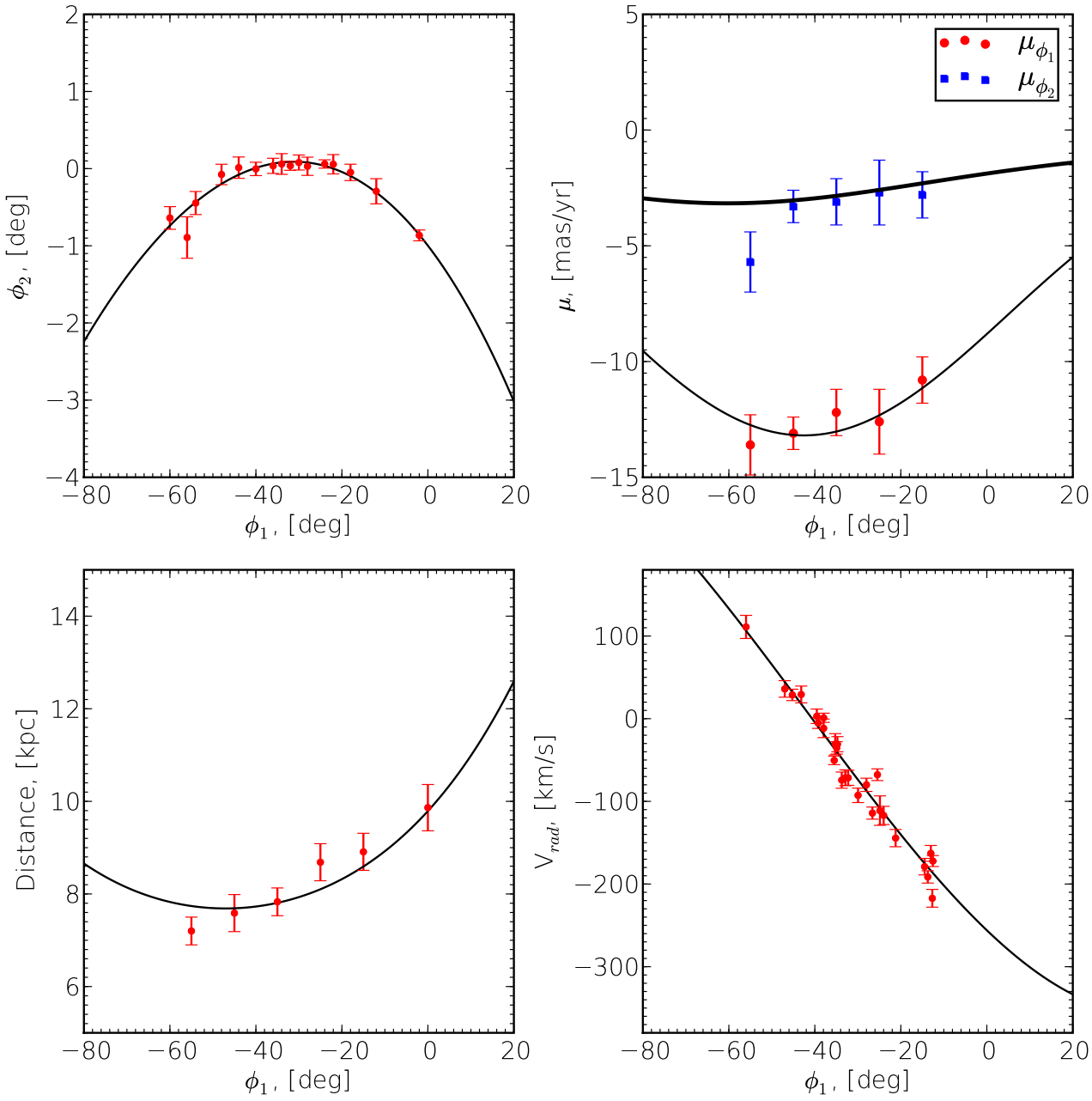

FIG. 13.— The data-model comparison for the best fit orbit in a flattened logarithmic potential (Eq. 5 with $V_c = 220$ km/s and q_Φ=0.9. The color data points with error bars shows the observational data, while the black lines show the model predictions for the orbit with $\vec{X}(0) = (-3.41, 13.00, 9.58)$ kpc, $\dot{\vec{X}}(0) = (-200.4, -162.6, 13.9)$ km/s. The top left panel shows the positions on the sky, the top right panel shows the proper motions, the bottom left panel shows the distances, the bottom right panel shows the radial velocities. On the top right panel, red circles and thin line show μ_{ϕ_1}, while blue squares and thick line show μ_{ϕ_2}.

with the information from GD-1 .

The fit shown in Fig. 14 asks the data not only to constrain the potential at the stream location and determine the stream orbit, but also to infer the Sun's motion (or at least V_{LSR}) from its reflex effect on the data. Clearly providing a prior on $V_c(R_0, 0)$ is sensible, especially if we care about constraints on the potential flattening. We consider the constraints that arise from the Sun's reflex motion with respect to the Galactic center the most robust and sensible prior in this context. Ghez et al. (2008) recently combined radio data (Reid & Brunthaler 2004) with near-IR data on the Galactic center kinematics to arrive at $V_c(R_0, 0) = 229 \pm 18$ km/s. It is also noticeable that our own constraint on $V_c(R_0, 0)$ from Fig. 14, 221^{+16}_{-20} km/s, is close both in value and uncertainty to the estimate of Ghez et al. (2008), which is based on a completely disjoint dataset and approach.

Fig. 15 shows the resulting log-likelihood contours and 1σ, 2σ, 3σ confidence regions after applying this prior on

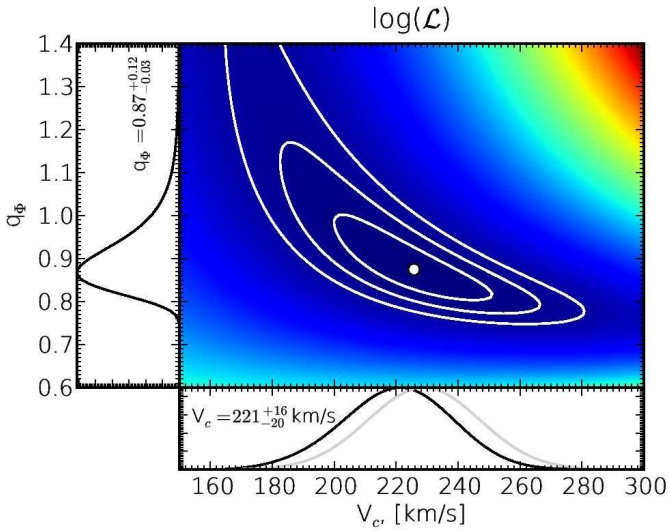

FIG. 14.— The log-likelihood surface of the orbit fit for the family of flattened logarithmic potentials (Eq. 5) with different circular velocities V_c and flattenings q_Φ with a flat prior on V_c. Note that V_c enters both into the model velocities of the stream stars and into the correction of all three velocity components for the Sun's motion. The contours show the 1σ, 2σ and 3σ confidence regions. The inset panels at the bottom and on the left show the 1D marginalized posterior probability distributions for V_c, q_Φ respectively. The gray line in the bottom panel shows the probability distribution for the V_c from Ghez et al. (2008), which we shall use as a prior in Fig. 15.

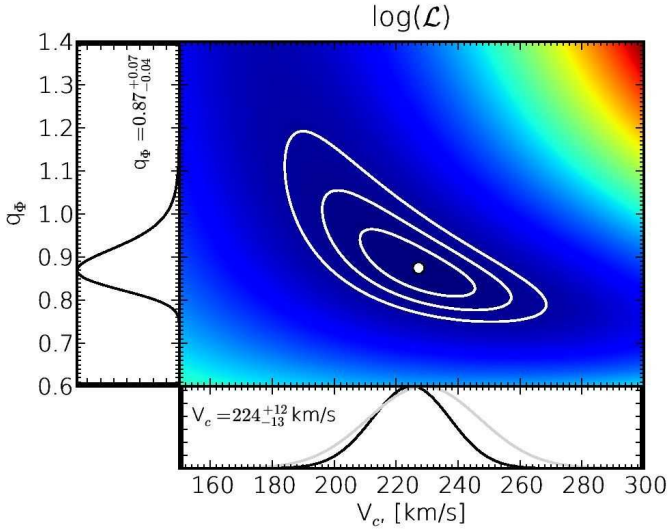

FIG. 15.— The log-likelihood surface of the orbit fit for the family of flattened logarithmic potentials (Eq. 5) with different circular velocities V_c and flattenings q_Φ, but now with a prior on the V_c of 229±18 km/s from Ghez et al. (2008). The likelihood was also marginalized over the Gaussian prior on $R_0 = 8.4 \pm 0.4$ kpc. As on Fig. 14 the contours show the 1σ, 2σ and 3σ confidence regions. The inset panels at the bottom and on the left show the 1D marginalized posterior probability distributions for V_c, q_Φ respectively. The gray line in the bottom panel shows the adopted prior distribution for the V_c from Ghez et al. (2008)

the V_c (229±18 km/s). Note that likelihood on Fig. 15 is also marginalized over R_0 with a Gaussian prior ($R_0 = 8.4 \pm 0.4$ kpc Ghez et al. 2008).

Fig. 15 shows that the posterior probability distribution on V_c has slightly changed to $V_c(R_0) = 224^{+12}_{-14}$ km/s with noticeably smaller error bar compared to the value

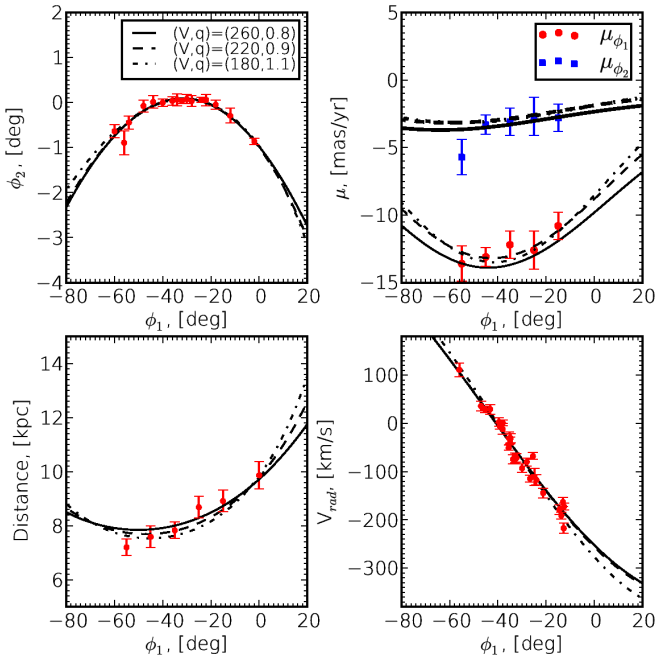

FIG. 16.— The data-model comparison for a set of best-fit orbits in different logarithmic potentials (Eq. 5) with three different (V_c, q_Φ) parameters values (180 km/s,1.1), (220 km/s,0.9), (260 km/s,0.8.) The colored data points with error bars show the observational data, while the black lines show the model predictions (different line styles show the orbit models in different potentials). The top left panel shows the positions on the sky, the top right panel shows the proper motions, the bottom left panel shows the distances, the bottom right panel shows the radial velocities. On the top right panel, red circles and thin lines show μ_{ϕ_1}, while blue squares and thick lines show μ_{ϕ_2}.

from Ghez et al. (2008). Fig 15 also shows us the slight improvement comparing to Fig. 14 of flattening constraints: $q_\Phi = 0.87^{+0.07}_{-0.04}$. This means that the *total* potential appears to be oblate (in the radial range probed); this may not be surprising, as the stellar disk – which is manifestly very flattened – contributes to the total potential.

Fig. 16 illustrates how well the best-fit orbits for different potentials $\Phi(\vec{X}|V_c, q_\Phi)$ can mimic one another other in the space of observables. This is the source of the parameter covariances shown in Fig. 14 and 15.

The fitting of the orbit shown in Fig. 13 allows us to make an estimate of the line-of-sight velocity dispersion in the stream, by comparing the dispersion of the radial velocity residuals with the accuracy of individual radial velocities. Assuming that without observational uncertainties the residuals from the orbit fit should be Gaussian distributed with zero mean we performed the maximum likelihood fitting of the residuals, which gives a 90% confidence upper limit on the velocity dispersion of stars in the stream of ~ 3 km/s.

Before we aim at separating possible flattening contributions from the halo and disk, it is worth commenting on the accuracy and limitations of our estimate of q_Φ. In the range $(R, z) \approx (12, 6)$ kpc no other direct observational constraints on the potential shape exist in the literature, and hence our estimate of $q_\Phi = 0.87^{+0.07}_{-0.04}$ is a new and important contribution. On the other hand, an error of $\delta q_\Phi \sim 0.05$, especially when translated into the

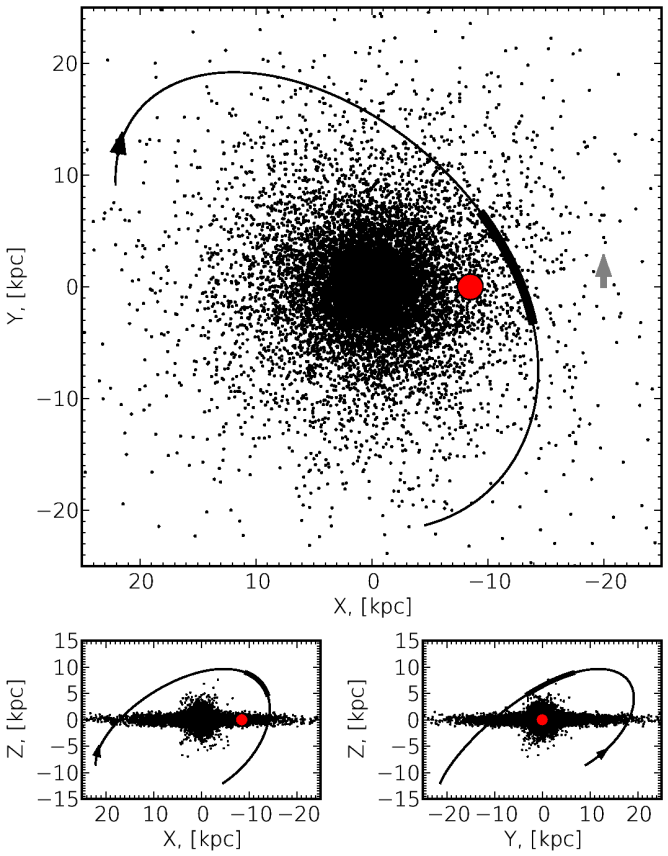

FIG. 17.— 2-D projections of the orbit in the Galactic rectangular coordinates. The position of the Sun is shown by a red circle. The Galaxy is shown by a cloud of points and the gray arrow shows the direction of the galactic rotation. The black arrow shows the direction of the orbital movement of the stream stars. The orbit is the best fit orbit for the $V_c = 220$ km/s, $q_\Phi = 0.9$ logarithmic potential(Eq. 5). The orbit for the 3-component potential(Eqns. 6, 7, 8) is almost undistinguishable from the orbit in logarithmic potential.

flattening error of the equivalent scale-free mass distribution, may not appear as particularly helpful in model discrimination, or as impressively accurate. Especially as a manifestly cold stellar stream spanning over 60° on the sky may seem ideal for mapping the potential at first glance.

5.2. *Constraints on the shape of the dark matter halo from a bulge, disk, halo 3-component potential*

In the previous section we constrained the parameters of a simplified MW potential, the spheroidal logarithmic potential. It is clear that the MW potential at the position of the stream must depend explicitly on the sum of baryonic Galaxy components (bulge and disk) and on the dark matter halo. We now explore whether our constraint on the shape of the overall potential, $q_\Phi \sim 0.9$, permits interesting statements about the shape of the DM potential itself. At the distance of $(R, z) \approx (12, 6)$ kpc the contribution of the disk to the potential should still be relatively large, weakening or at least complicating inferences on the shape of the DM distribution.

We adopt a three-component model of the Galaxy potential, choosing one that is widely used in the modeling of the Sgr stream (Helmi 2004; Law et al. 2005; Fellhauer et al. 2006) and reproduces the galactic rotation curve reasonably well.

The model consists of a halo, represented by the logarithmic potential The numerical values of parameters of the potential were taken from Fellhauer et al. (2006)

$$\Phi_{halo}(x,y,z) = \frac{v_{halo}^2}{2} \ln\left(x^2 + y^2 + \left(\frac{z}{q_{\Phi,halo}}\right)^2 + d^2\right), \quad (6)$$

where we have adopted $d = 12$ kpc from the previous authors. The disk is represented by a Miyamoto-Nagai potential (Miyamoto & Nagai 1975),

$$\Phi_{disk}(x,y,z) = \frac{GM_{disk}}{\sqrt{x^2 + y^2 + (b + \sqrt{z^2 + c^2})^2}} \quad (7)$$

with $b = 6.5$ kpc, $c = 0.26$ kpc. The bulge is modeled as a Hernquist potential:

$$\Phi_{bulge}(x,y,z) = \frac{GM_b}{r + a} \quad (8)$$

with $M_b = 3.4 \times 10^{10} M_\odot$, $a = 0.7$ kpc

As in the previous section, for any given set of potential parameters, we can find the best-fitting stream orbit and compute χ^2 of the fit. In the current paper we do not make any attempts to fully fit all the parameters of the MW potential, but we try to make an estimate of the MW DM halo flattening. We take the 3-component potential and fix all but 3 parameters — disk mass M_{disk}, circular velocity of the halo v_{halo} and the flattening of the halo $q_{\Phi,halo}$. On a 3-D grid of these parameters we perform a χ^2 fit. Figure 18 shows the results of such fit after marginalization over the orbital parameters $(\vec{X}(0), \dot{\vec{X}}(0))$, circular velocity of the halo v_{halo} with a Gaussian prior from Xue et al. (2008) and a Gaussian prior on the circular velocity at the Sun's radius from Ghez et al. (2008). The Figure clearly illustrates that in the case of the 3-component potential, the current data is unable to give a significant new insights on the flattening of the DM halo. We can only say that at 90% confidence $q_{\Phi,halo} > 0.89$. We note however that for the future analysis, if a multi-component model for the potential is used then more prior information is required, i.e. not only on V_{LSR} and v_{halo} but on M_{disk} and other parameters of the potential.

6. DISCUSSION AND CONCLUSIONS

In this paper we have presented a thorough analysis the GD-1 stream combining the publicly available SDSS and SEGUE data with follow-up spectroscopic observations from Calar Alto. The combination of the photometric SDSS observations, USNO-B/SDSS proper motions, SDSS, SEGUE and Calar Alto radial velocities allowed us to construct a unprecedented 6-D phase-space map of this very faint (29 mag/sq. arcsec) tidal stream. The 6-D phase-space map of the stream, spanning more than 60° on the sky, provided the opportunity not only to fit the orbit as Grillmair & Dionatos (2006b) and Willett et al. (2009) have done previously but to explore what constraints can be placed on the MW potential.

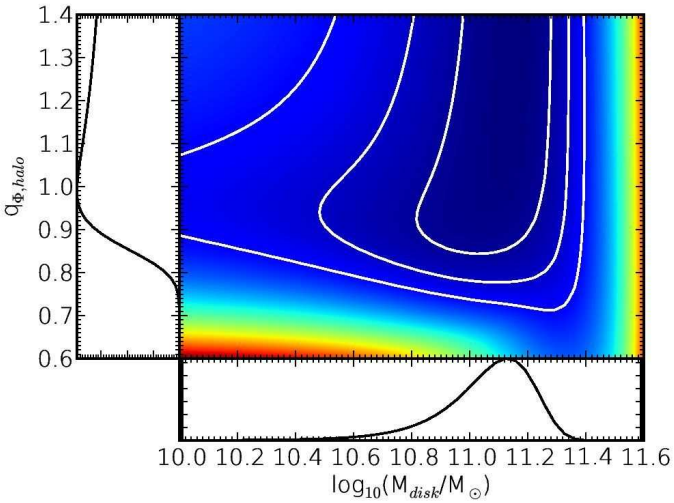

FIG. 18.— The log-likelihood surface of the orbit fit for a 3-component potential (Eq. 6, 7 and 8) with different disk masses M_{disk}, halo circular velocities v_{halo} and halo flattenings $q_{\Phi,halo}$. The likelihood was marginalized over the circular velocity of the halo v_{halo} with the Gaussian prior on $v_{halo} = 170 \pm 15$ km/s from Xue et al. (2008) and the Gaussian prior on $V_{LSR} = 229 \pm 18$ km/s) from Ghez et al. (2008) . The contours show the 1σ, 2σ and 3σ confidence regions. The inset panels at the bottom and on the left show the 1D marginalized posterior probability distributions for M_{disk}, $q_{\Phi,halo}$ respectively.

The analysis is based on the assumption that the stream stars occupy one orbit. In detail, of course, different stars on the stream have slightly different values of conserved quantities and therefore lie on slightly different orbits. Effectively, our analysis depends on these being small when compared with an orbital uncertainties. The magnitude of the departure of the stream from a single orbit will, in detail, be a function of the projenitor and the distruption process; as these details became understood the model can be refined.

We found that the distribution of stream stars in phase space can be well fit by an inclined eccentric orbit in the spheroidal logarithmic potential. After marginalization over the stream orbital parameters we derive a circular velocity $V_c = 221^{+16}_{-20}$ km/s and flattening $q_\Phi = 0.87^{+0.12}_{-0.03}$. This measurement has been made without the use of any information other than that in the GD-1 stream itself. It is important that the information available in the observations of the stream is very sensitive to the V_c, the circular velocity at the Sun's position. The reason for that is that the stream extends more then 60° on the sky and therefore both the radial velocities and the proper motions have components coming from the projection of the Sun's motion.

If we combine our circular velocity measurement with existing prior on the V_c from Ghez et al. (2008) and also marginalize over the distance from the Sun to the Galactic center using the Ghez et al. (2008) prior ($R_0 = 8.4 \pm 0.4$ kpc), we further tighten the error bar on $V_c = 224^{+12}_{-13}$ km/s and on the flattening of the potential $q_\Phi = 0.87^{+0.07}_{-0.04}$. Our measurement of the V_c is the best constraint to date on the circular velocity at the Sun's position, and the measurement of q_Φ is the only strong constraint on q_Φ at galactocentric radii near $R \sim 15$ kpc.

The measurement of the flattening of the potential $q_\Phi = 0.87^{+0.07}_{-0.04}$ describes only the flattening of the overall Galaxy potential at the stream's position $(R, z) \approx (12, 6)$ kpc where the disk contribution to the potential is presumably large. Unfortunately the data on the GD-1 stream combined with the Ghez et al. (2008), Xue et al. (2008) priors on V_c and v_{halo} are not enough for separating the flattening of the halo from the flattening of the total Galaxy potential. So we are unable to place strong constraints on flattening of the MW DM halo; we put a 90% confidence lower limit at $q_{\Phi,halo} > 0.89$.

Despite the negative result on the measurement of the MW DM halo flattening, we note that the data from the GD-1 stream is able to give strong constraints on two important Galaxy parameters. We claim that that our dataset on the GD-1 stream should now be combined with other available MW kinematical data (from other stellar streams, BHBs, MW rotation curve) in order to tighten the existing constraints on the Galaxy parameters. It is important that the constraints on Galaxy potential based on the GD-1 stream dataset are, to large extent, model-independent and purely kinematic i.e. the constraints on the V_c come to large extent from the projection effects and manifest themselves in proper motions and radial velocities.

We think that it is quite surprising that such a long (60°) stream with full 6-D map didn't allow us to contrain large number of parameters of the MW DM halo and other Galactic components. We think that there are several reasons for that, but the most important is that while the observed part of the orbit spans $\sim 70°$ on the sky from the Sun's point of view, the orbital phase spanned by the stars as seen from the Galactic center, is only $\sim 40°$. Furthermore, the observable part of the stream occupies the perigalacticon part of the orbit, so the range of Galactocentric distances probed by the stream is small. That makes it plausible why orbits of different eccentricities, and hence of different azimuthal velocities at their pericenter, can match so closely the same set of 6-D coordinates. Since very cold streams take many orbits to spread a substantial fraction of 2π in orbital phase (see e.g. also Pal 5; Odenkirchen et al. 2001; Grillmair & Dionatos 2006a), all future analyses of yet-to-be discovered streams will particularly need to consider the trade-off between the conceptual and practical attractiveness of 'cold' streams and the near-inevitable limitations of their phase coverage.

In addition to the weakness coming from phase coverage, our analysis at this point must rely on photometric distance estimates; these have random errors of $\sim$10%, after an empirical distance correction to the best fit isochrones that is of the same magnitude (see Section 2). While the proper motions that we derived for ensembles of stream stars are unprecedented for a stellar stream in the Milky Way's outer halo; yet, the corresponding velocity precision, especially when compounded by distance errors, is still the largest single source of uncertainty in the fitting (e.g. our tests have shown that overestimating heliocentric distances to the stream leads to the overestimated measurement of V_c). Both the deficiencies of the distances and proper motions on GD-1 will be largely alleviated after the launch of the Gaia satellite, which will allow much tighter constraints on the Galactic

potential.

But before the launch of Gaia, we suggest that further observations of radial velocities of stars in the stream (with deeper spectroscopy) and improvements in proper motion precision (with e.g. Pan-STARRS Kaiser et al. 2002) should be able to reduce the error bars on Galaxy parameters significantly. It is also important to calibrate properly the distance to the stream, which may be done by confirming several probable BHB candidates in the stream.

We suggest that any attempt to fit the Galactic potential(such as Widrow et al. 2008) now should not ignore the dataset on GD-1 and should incorporate it into their fits.

The orbital parameters, which we have measured for the GD-1 stream, are more or less consistent with those from Willett et al. (2009): pericenter is at 14 kpc from the GC, the apocenter is at 26 kpc, the orbit inclination with respect to the Galactic plane is 39°. We have also estimated the total stellar mass associated with the stream to be $\sim 2 \times 10^4 M_\odot$, which together with the relatively small stream width of ~ 20 pc suggests that the progenitor of the stream was a globular cluster, although we cannot completely rule out the dwarf galaxy progenitor. We have also determined the 90% confidence upper limit for the velocity dispersion of the stars in the stream ~ 3 km/s which do not contradict significantly neither globular cluster nor dwarf galaxy progenitor hypothesis. Given the length of the observable part of the stream of ~ 10 kpc, and the velocity dispersion $\lesssim 3$ km/s the age of the stream can be estimated to be greater than 1.5 Gyrs (assuming that the progenitor is in the middle of the observed part of the stream). It is interesting that the stream managed to evade possible destruction by interaction with DM subhalos orbiting around MW (Carlberg 2009). Although the clumpiness observed in the stream may be attributed to these past interactions (Koposov et al 2010 in prep.).

Overall in this paper we have illustrated a method of analyzing the thin stellar stream using all the available information on it and further utilizing that to constrain the Galaxy potential. We believe that in the epoch of Pan-STARRS, LSST and especially Gaia, which will give us a wealth of new information on the MW halo, stream-fitting like that presented in this paper will be extremely useful and productive.

SK was supported by the DFG through SFB 439, by a EARA-EST Marie Curie Visiting fellowship and partially by RFBR 08-02-00381-a grant. SK acknowledges hospitality from the Kavli Institute for Theoretical Physics (KITP) Santa Barbara during the workshop "Building the Milky Way". SK thanks Jelte de Jong for running MATCH code on the GD-1 data and the Calar Alto observing staff for excellent support. DWH acknowledges support from NASA (grant NNX08AJ48G) and a Research Fellowship from the Alexander von Humboldt Foundation. The authors thank Kathryn Johnston, Jorge Peñarubia, James Binney for useful discussions and the anonymous referee for the elaborated referee report which helped us improve the paper.

The project made use the open-source Python modules matplotlib, numpy, scipy; SAI Catalogue Access Services (Sternberg Astronomical Institute, Moscow, Russia)(Koposov et al. 2007b); NASA's Astrophysics Data System Bibliographic Services.

The SDSS is managed by the Astrophysical Research Consortium for the Participating Institutions. The Participating Institutions are the American Museum of Natural History, Astrophysical Institute Potsdam, University of Basel, University of Cambridge, Case Western Reserve University, University of Chicago, Drexel University, Fermilab, the Institute for Advanced Study, the Japan Participation Group, Johns Hopkins University, the Joint Institute for Nuclear Astrophysics, the Kavli Institute for Particle Astrophysics and Cosmology, the Korean Scientist Group, the Chinese Academy of Sciences (LAMOST), Los Alamos National Laboratory, the Max-Planck-Institute for Astronomy (MPIA), the Max-Planck-Institute for Astrophysics (MPA), New Mexico State University, Ohio State University, University of Pittsburgh, University of Portsmouth, Princeton University, the United States Naval Observatory, and the University of Washington.

APPENDIX

TRANSFORMATION OF EQUATORIAL COORDINATES TO STREAM COORDINATES ϕ_1, ϕ_2

$$\begin{pmatrix} \cos(\phi_1)\cos(\phi_2) \\ \sin(\phi_1)\cos(\phi_2) \\ \sin(\phi_2) \end{pmatrix} = \begin{pmatrix} -0.4776303088 & -0.1738432154 & 0.8611897727 \\ 0.510844589 & -0.8524449229 & 0.111245042 \\ 0.7147776536 & 0.4930681392 & 0.4959603976 \end{pmatrix} \times \begin{pmatrix} \cos(\alpha)\cos(\delta) \\ \sin(\alpha)\cos(\delta) \\ \sin(\delta) \end{pmatrix}$$

REFERENCES

Abazajian, K. N., et al. 2009, ApJS, 182, 543
An, D., et al. 2008, ApJS, 179, 326
Belokurov, V., et al. 2006, ApJ, 642, L137
Belokurov, V., et al. 2007, ApJ, 657, L89
Belokurov, V., et al. 2007, ApJ, 658, 337
Belokurov, V., et al. 2007, ApJ, 654, 897
Binney, J., & Tremaine, S. 1987, Princeton, NJ, Princeton University Press, 1987, 747 p.,
Brand, J., & Blitz, L. 1993, A&A, 275, 67
Carlberg, R. G. 2009, ApJ, 705, L223
Carollo, D., et al. 2007, Nature, 450, 1020
Cash, W. 1979, ApJ, 228, 939
Chabrier, G. 2001, ApJ, 554, 1274
Cole, N., et al. 2008, ApJ, 683, 750
Cox D., & Hinckley D. 1974, Theoretical Statistics, Chapman and Hall
de Jong, J. T. A., Rix, H.-W., Martin, N. F., Zucker, D. B., Dolphin, A. E., Bell, E. F., Belokurov, V., & Evans, N. W. 2008, AJ, 135, 1361
Dehnen, W., & Binney, J. J. 1998, MNRAS, 298, 387
Dehnen, W., Odenkirchen, M., Grebel, E. K., & Rix, H.-W. 2004, AJ, 127, 2753
Dolphin, A. E. 2002, MNRAS, 332, 91
Eyre, A., & Binney, J. 2009, arXiv:0907.0360

Eyre, A. 2009, arXiv:0912.1896
Fellhauer, M., et al. 2006, ApJ, 651, 167
Ghez, A. M., et al. 2008, ApJ, 689, 1044
Gillessen, S., Eisenhauer, F., Trippe, S., Alexander, T., Genzel, R., Martins, F., & Ott, T. 2009, ApJ, 692, 1075
Girardi, L., Bressan, A., Bertelli, G., & Chiosi, C. 2000, A&AS, 141, 371
Grillmair, C. J., Freeman, K. C., Irwin, M., & Quinn, P. J. 1995, AJ, 109, 2553
Grillmair, C. J. 2006, ApJ, 645, L37
Grillmair, C. J., & Dionatos, O. 2006, ApJ, 641, L37
Grillmair, C. J., & Dionatos, O. 2006, ApJ, 643, L17
Grillmair, C. J., & Johnson, R. 2006, ApJ, 639, L17
Grillmair, C. J. 2009, ApJ, 693, 1118
Ibata, R., Lewis, G. F., Irwin, M., Totten, E., & Quinn, T. 2001, ApJ, 551, 294
Irwin, M. J., et al. 2007, ApJ, 656, L13
Ivezić, Ž., et al. 2008, ApJ, 684, 287
Johnston, K. V., Law, D. R., & Majewski, S. R. 2005, ApJ, 619, 800
Helmi, A. 2004, MNRAS, 351, 643
Kaiser, N., et al. 2002, Proc. SPIE, 4836, 154
Koposov, S., et al. 2007, ApJ, 669, 337
Koposov, S., Bartunov, O., Belinskiy, A., & Karpov, S. 2007, Astronomical Data Analysis Software and Systems XVI, 376, 34
Küpper, A. H. W., Kroupa, P., Baumgardt, H., & Heggie, D. C. 2010, MNRAS, 401, 105
Lampton, M., Margon, B., & Bowyer, S. 1976, ApJ, 208, 177
Law, D. R., Johnston, K. V., & Majewski, S. R. 2005, ApJ, 619, 807
Marigo, P., Girardi, L., Bressan, A., Groenewegen, M. A. T., Silva, L., & Granato, G. L. 2008, A&A, 482, 883
Markwardt, C. B. 2009, arXiv:0902.2850
Marquardt, D. W. 1963, Journal of the Society for Industrial and Applied Mathematics, 11, 431
Miyamoto, M., & Nagai, R. 1975, PASJ, 27, 533
Monet, D. G., et al. 2003, AJ, 125, 984
Munn, J. A., et al. 2004, AJ, 127, 3034
Munn, J. A., et al. 2008, AJ, 136, 895
Nash, S. G., 1984, SIAM J. Numer. Anal. 21, 770
Newberg, H. J., et al. 2002, ApJ, 569, 245
Odenkirchen, M., et al. 2001, ApJ, 548, L165
Odenkirchen, M., et al. 2003, AJ, 126, 2385
Odenkirchen, M., Grebel, E. K., Kayser, A., Rix, H.-W., & Dehnen, W. 2009, AJ, 137, 3378
Perryman, M. A. C., et al. 2001, A&A, 369, 339
Prugniel, P., Soubiran, C., Koleva, M., & Le Borgne, D. 2007, arXiv:astro-ph/0703658
Reid, M. J., & Brunthaler, A. 2004, ApJ, 616, 872
Reid, M. J., et al. 2009, arXiv:0902.3913
Rockosi, C. M., et al. 2002, AJ, 124, 349
Walsh, S. M., Jerjen, H., & Willman, B. 2007, ApJ, 662, L83
Widrow, L. M., Pym, B., & Dubinski, J. 2008, ApJ, 679, 1239
Willett, B. A., Newberg, H. J., Zhang, H., Yanny, B., & Beers, T. C. 2009, ApJ, 697, 207
Xue, X. X., et al. 2008, ApJ, 684, 1143
Yanny, B., et al. 2009, AJ, 137, 4377